Nanoscale
Advances

ROYAL SOCIETY
OF CHEMISTRY

COMMUNICATION

View Article Online
View Journal | View Issue

Check for updates

Cite this: *Nanoscale Adv.*, 2025, 7, 5956

Received 15th July 2025
Accepted 23rd August 2025

DOI: 10.1039/d5na00683j

rsc.li/nanoscale-advances

Supersonic cluster beam deposition of bimetallic Sn–Pt nanogranular films: nanostructure control, segregation, and 2D intermetallic phases

José Enrique Martinez Medina,[ab] Marc Heggen,[c] Adrian-Marie Philippe[b] and Emanuele Barborini *[b]

Nanogranular films obtained by the soft assembly of atomic clusters feature functional properties that are of interest in a variety of fields, ranging from gas sensing to neuromorphic computing, heterogeneous catalysis and the biomedical sector. Bimetallic nanogranular films, combining a post-transition metal (tin) and a catalytic metal (platinum), were produced using supersonic cluster beam deposition. By operating the cluster source with a double-rod cathode or sintered cathode configuration, completely different nanostructures were obtained. In the first case, segregated particle families of the two metals with their specific size distributions were observed, while in the second case, the formation of 2D layered intermetallic Sn–Pt phases embedded into Sn nanoparticles was observed. These phases are compatible with the Dirac nodal arc semimetal $PtSn_4$. Chemoresistive hydrogen gas sensing measurements are reported as an example of prospective application of nanogranular films containing segregated SnO_x and Pt nanoparticle families.

Introduction

Nanogranular metallic films are systems formed by the soft assembling of nanoparticles that maintain their individuality to a large degree, with only a small area of points of contact with each other. Their properties stem from this structure, and include nanoporosity and reduced density with respect to the bulk counterpart;[1,2] distinct electrical transport, exhibiting both a resistivity that is orders of magnitude larger than the bulk counterpart and resistive switching phenomena;[3–5] and surface morphological features and roughness in the proper length scale range to trigger mechano-transduction effects in cells.[6] These characteristics form the basis of several metal or metal oxide nanogranular film applications in the areas of chemoresistive gas sensing,[7] neurosignal recording,[8,9] biological sample processing,[10,11] heterogeneous catalysis[12,13] and neuromorphic computing.[14]

In the last two decades, Supersonic Cluster Beam Deposition (SCBD) equipped with the Pulsed Microplasma Cluster Source (PMCS) has been demonstrated as one of the most powerful and versatile techniques for investigating nanogranular films in all the abovementioned areas.[15] This success mainly stems from it being a room-temperature, high-vacuum, physical deposition process, featuring excellent material purity, the absence of chemical terminations at the cluster surface, and full compatibility with any kind of substrate, including mechanically delicate ones, such as micromachined device platforms, and thermolabile ones, such as soft polymers.

The nanogranular films involved in the research mentioned are all made of a single metal, or a metal oxide, with a material portfolio including most of the transition metals: Ti, Zr, Hf, V, Nb, Cr, Mo, W, Fe, Ru, Co, Ir, Ni, Pd, Pt, Cu, Ag, Au, as well as C and Sn. Despite their importance for understanding gas aggregation processes and related cluster structures (core–shell, Janus, intermetallic phases, *etc.*), bimetallic systems have been little investigated with SCBD based on PMCS. Among the few examples, it is worth mentioning the recent work of S. Osmani *et al.* on bismuth ferrite oxides (BFO), where the authors use a BiFe 50 : 50 at% cathode in PMCS and claim the formation of the phase $Bi_{24}Fe_2O_{39}$, whose photo-electrochemical properties are then investigated;[13] and the work of F. Vega *et al.* on Ag–Rh, where the authors use a properly sintered cathode to obtain nanogranular bimetallic films with 75 : 25 at% composition in order to study their hydrogen absorption properties.[16]

In this article, we report on the bimetallic Sn–Pt nanogranular films deposited by SCBD. The initial motivation for this combination of materials is related to chemoresistive gas sensing, an applicative area in which tin oxide is the "reference" material. In this regard, a nanogranular structure integrating tin oxide with a catalytic material such as Pt is expected to exhibit enhanced gas detection performances. We demonstrate

---

[a] *Department of Physics and Materials Science, University of Luxembourg, Esch-Sur-Alzette, Luxembourg*

[b] *Luxembourg Institute of Science and Technology (LIST), 41 Rue du Brill, L-4422 Belvaux, Luxembourg. E-mail: emanuele.barborini@list.lu*

[c] *Ernst Ruska-Centre for Microscopy and Spectroscopy with Electrons (ER-C), Forschungszentrum Jülich GmbH, Jülich, Germany*

that, by altering the cathode configuration within the cluster source, entirely different film nanostructures are obtained. For "double rod" cathodes, two segregated families of nanoparticles are obtained for Sn and Pt, while for sintered cathodes, a distinct nanostructure is observed, in which a 2D-layered intermetallic Sn–Pt phase is present within Sn nanoparticles, breaking their spheroidal symmetry. Upon structural analysis, this phase is identified as $PtSn_4$, an intermetallic compound known to have a Dirac nodal arc semimetal nature.[17,18] To the best of our knowledge, this is the first time that the spontaneous formation of $PtSn_4$ phase within Sn nanoparticles has been observed in a gas-phase physical deposition process.

Materials and methods

Despite design revisions and a substantial engineering upgrade, the principle of operation of the Pulsed Microplasma Cluster Source (PMCS) did not change from its first iteration.[19] Fig. 1 shows the sequence of the basic physical phenomena leading to the formation of a nanogranular film by SCBD, starting from a solid-state precursor. The figure includes the qualitative evolution of the velocity distribution characterizing the motion of the clusters (thin black arrows), the velocity of the centre of mass of the moving group of clusters (v_{CM}), and the temperature profile observed in the centre of mass. The method implements a gas aggregation process by synchronizing a pulsed electrical discharge with a pulsed jet of inert gas that acts first as a sputtering promoter of the metallic precursor rod (cathode), in the form of a localized plasma plume (localized sputtering in Fig. 1). Successively, the inert gas acts as a thermal bath for metallic atoms to cool down and aggregate in nanoparticles (nucleation and growth), before finally operating the extraction of the nanoparticles from the source towards the deposition chamber through a nozzle gas expansion. The local temperature throughout the process is expected to (i) reach very high values during the pulsed discharge; (ii) decrease during the nucleation and growth step as a consequence of the thermalization by the inert gas; (iii) drop suddenly due to the isentropic character of supersonic expansion; and (iv) finally return to room temperature at the deposition.

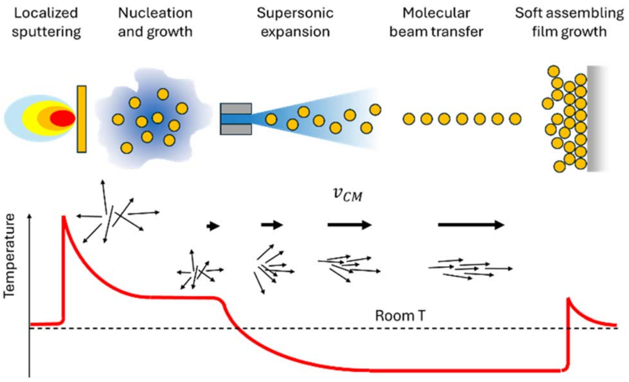

Fig. 1 Principle of operation of the Pulsed Microplasma Cluster Source (PMCS), showing the sequence of the basic physical phenomena leading to the formation of a nanogranular film. Thin arrows represent the velocity vectors of the clusters, while the thick v_{CM} arrow represents the velocity of the centre of mass. The red curve represents the temperature associated with the translational movement and observed in the centre of mass.

In this work, we operated the PMCS with two configurations for the cathode: a "double rod" one, where high purity rods of Sn and Pt (Goodfellow) were brought into contact each other, with the interface aligned with the plasma jet centreline (Fig. 2); and a sintered cathode one with an Sn–Pt composition of 85–15 at%. The cluster source was backed with argon process gas at a pressure of 40 bar, supporting pulsed gas injections with a nominal duration of around 200 µs. Synchronized with the gas injection, the pulsed electrical discharge was operated at a voltage of 500 V with a current pulse duration of 30 µs. The whole system ran at a repetition rate of 4 pulses per second, with a base pressure of 5×10^{-8} mbar in the deposition chamber at source off. In a "double rod" configuration, the erosion of the cathode pair shows a Gaussian-like profile cantered at the interface of the two materials with a FWHM of about 1.5 mm (Fig. 2c).

Transmission electron microscopy (TEM) was conducted on a Jeol JEM-F200 cold FEG operating at 200 kV and on Cs-image corrected FEI TITAN 80–300 microscope at 300 kV. In addition, high-angle-annular-dark-field scanning transmission electron microscopy (HAADF-STEM) was performed on a Hitachi HF5000 equipped with a spherical-aberration probe corrector operated at 200 kV. Elemental analysis by energy dispersive X-ray (EDX) analysis was conducted using an Aztec system with two Ultim Max Silicon Drift Detectors (Oxford Instruments, Abingdon, UK). Samples for structural and compositional investigations by TEM and STEM-EDX were deposited on standard TEM grids with a properly adjusted deposition time in order to obtain low-coverage, limited coalescence samples, enabling the clear identification of the single nanoparticles. Samples for electrical transport measurements in a reactive atmosphere (gas sensing) were prepared on interdigitated electrodes (IDEs), as reported in Martinez Medina *et al.*[4] In this case, a rastering protocol was implemented including a quartz crystal microbalance (Inficon

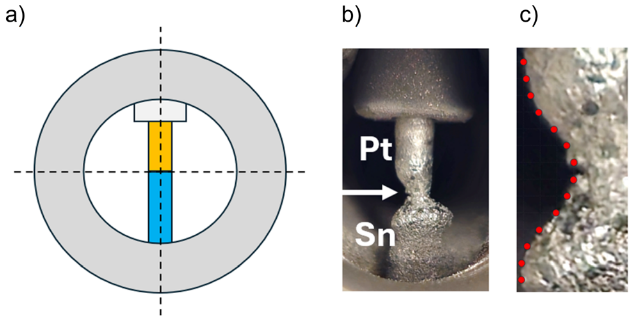

Fig. 2 (a) "Double rod" cathode configuration, where the two rods of Sn and Pt come into contact with each other, aligning the interface with the source centreline. (b) Image of the cathode after source operation, with the arrow highlighting the point of erosion. (c) Zoomed-in view of image (b), showing the Gaussian-like profile of the erosion.

SQM-160) positioned beside the IDEs for real-time monitoring of the deposited thickness.

Hydrogen gas sensing measurements were carried out on a custom-made test bench, which included a mass flow controllers (MFCs) based gas mixing system (Bioage G-MIX-5CH), a test chamber equipped with four micromanipulators for electrical contact (Linkam), and an electrometer acting as voltage source and current reader (Keithley 2614B).

Results

Segregated Sn–Pt nanoparticle families

The "double rod" cathode configuration generates a nanogranular film where two particle families of the two species, Pt and Sn, coexist as if the film were the result of a co-deposition. Fig. 3a shows a HAADF-STEM image of a low-coverage sample, where smaller objects with bright white contrast are visible alongside larger objects with weaker grey contrast. Elemental composition maps using EDX (Fig. 3b and c) identify the former as Pt nanoparticles and the latter as Sn oxide nanoparticles. Fig. 3d shows a high-resolution TEM image where one particle of each species is visible in detail. The Pt particle (white arrow) shows a well-defined crystalline lattice, while the uniform contrast of the Sn particle is consistent with the amorphous nature of Sn oxide already observed in small Sn nanoparticles by SCBD.[20]

Within the Sn particle family, core–shell structures are observed in larger particles. Core–shell structures originate from the Cabrera–Mott oxidation, which leaves the unreacted metallic β-Sn phase in the core surrounded by an SnO_x shell.

The presence of core–shell structures in larger Sn particles, as well as the observation of a uniform contrast in smaller particles, matching that of shells and suggesting full oxidation, and the evidence of partial coalescence occurring among nanoparticles are all in line with our recent results on the structure of SnO_x nanoparticles by SCBD and of the nanogranular films obtained by Sn nanoparticle soft assembling.[4,20,21]

The dimensions of the Sn and Pt nanoparticles align with previous observations for each single material, the size distributions of which are reported in Fig. 4. In both cases, histograms are fitted with a log-normal curve describing the size distribution of particles from gas-aggregation processes, as the one governing the growth of nanoparticles in PMCS.[22,23] Log-normal fitting returns a distribution mean of 7.0 nm and 2.0 nm for Sn and Pt, respectively.

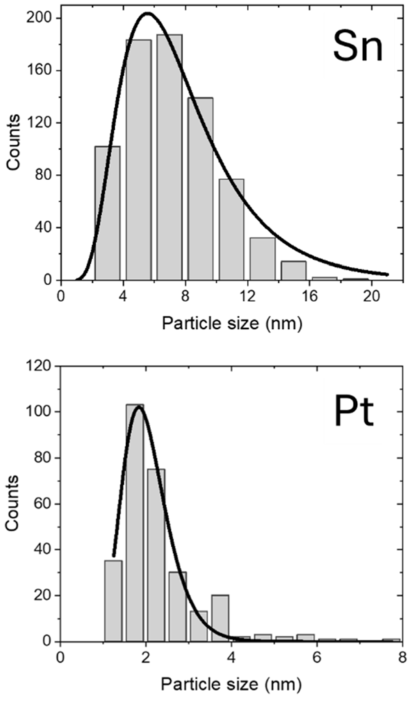

Fig. 4 Size distributions of Sn and Pt clusters. In both cases, histograms are fitted with a log-normal curve, returning a distribution mean of 7.0 nm and 2.0 nm for Sn and Pt, respectively.

The observation of two separated nanoparticle families suggests that each sputtering pulse within the cluster source is localized on one or the other of the metal rods, otherwise intermetallic or generically particles with mixed composition would have been present. Therefore, at least in the case of these materials, the width of the Gaussian-like erosion profile (Fig. 2c) must not be intended as the dimension of the single erosion event, but rather as representative of the random distribution along the centreline of much smaller erosion events occurring with the same probability on the Sn rod or on Pt rod.

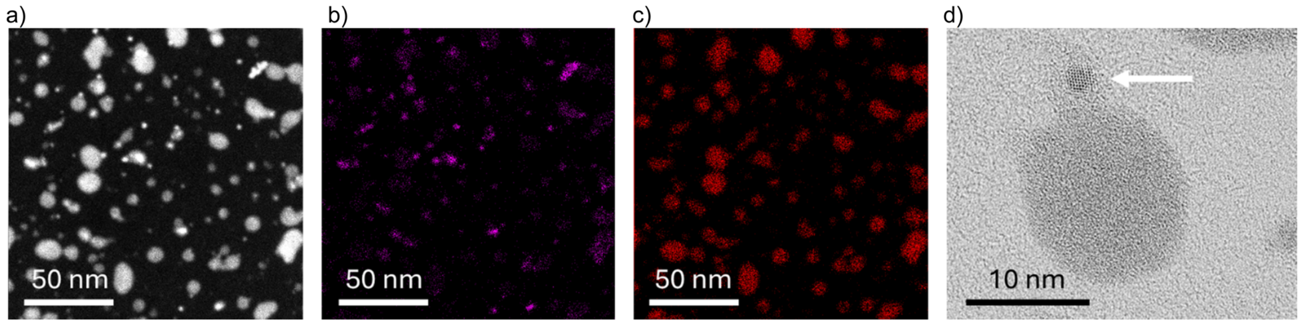

Fig. 3 (a) HAAD-STEM image of the material obtained with the "double rod" cathode configuration, showing segregated particle families: smaller, bright contrast particles, and larger, weak grey contrast particles. (b) STEM-EDX map of Pt. (c) STEM-EDX map of Sn. (d) High-resolution TEM image showing one Sn oxide particle and one Pt particle (white arrow).

Interparticle 2D phases

In contrast to the "double rod" cathode configuration, the sintered cathode one generates nanogranular films where the two metal species are present within each single nanoparticle, as shown in the STEM-EDX maps of Fig. 5. High-resolution TEM images, however, unveil segregated 2D layered domains in many of the particles (Fig. 5d). High-angle annular-dark-field (HAADF) STEM images confirm such 2D domains to be clearly segregated elements embedded into nanoparticles, breaking their spheroidal symmetry (Fig. 5e–h). Core–shell structures visible in the larger particles and originating from the Cabrera–Mott oxidation have been already commented on.

From high magnification EDX maps, the material composition in terms of Sn–Pt at% ranges from 94–6 to 84–16 at%, in line with the composition of the sintered cathode (85–15 at%) and the larger sputtering rate of Sn with respect to Pt. The composition of the bimetallic vapour originating from the sputtering of the sintered cathode (step 1 in Fig. 1) is therefore positioned in the region of the Sn–Pt phase diagram where the coexistence of the metallic β-Sn phase and intermetallic $PtSn_4$ phase is the thermodynamically favoured condensed configuration.[24] In line with this, the interparticle distribution of Sn and Pt shows a remarkable segregation, where the former is uniformly distributed while the latter accumulates in correspondence with the layered domains with a bright contrast (Fig. 6).

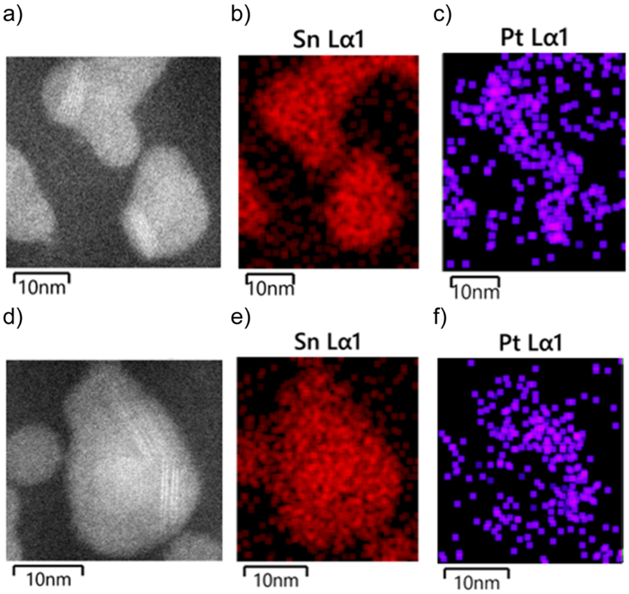

Fig. 6 (a–c) EDX-STEM analysis of the particle in Fig. 5e: HAADF-STEM image (a), tin distribution based on Sn-Lα1 (b) and platinum distribution based on Pt-Lα1 (c). (d–f) EDX-STEM analysis of the particles in Fig. 5g. In all cases, while tin appears to be distributed uniformly, platinum tends to segregate, and its distribution is correlated with the brightly contrasting layered structures.

Fig. 7 shows high-resolution STEM images of the particles shown in Fig. 5e and f. We identify a (almost) square-like pattern in the centre of the nanoparticle with 2.8 and 2.9 Å lattice spacing and distinct, brightly contrasting layered domains with a 5.8 and 4.4 Å lattice parameter.

The analysis of the high-resolution images unveils the presence of the $PtSn_4$ intermetallic phase oriented along (101)

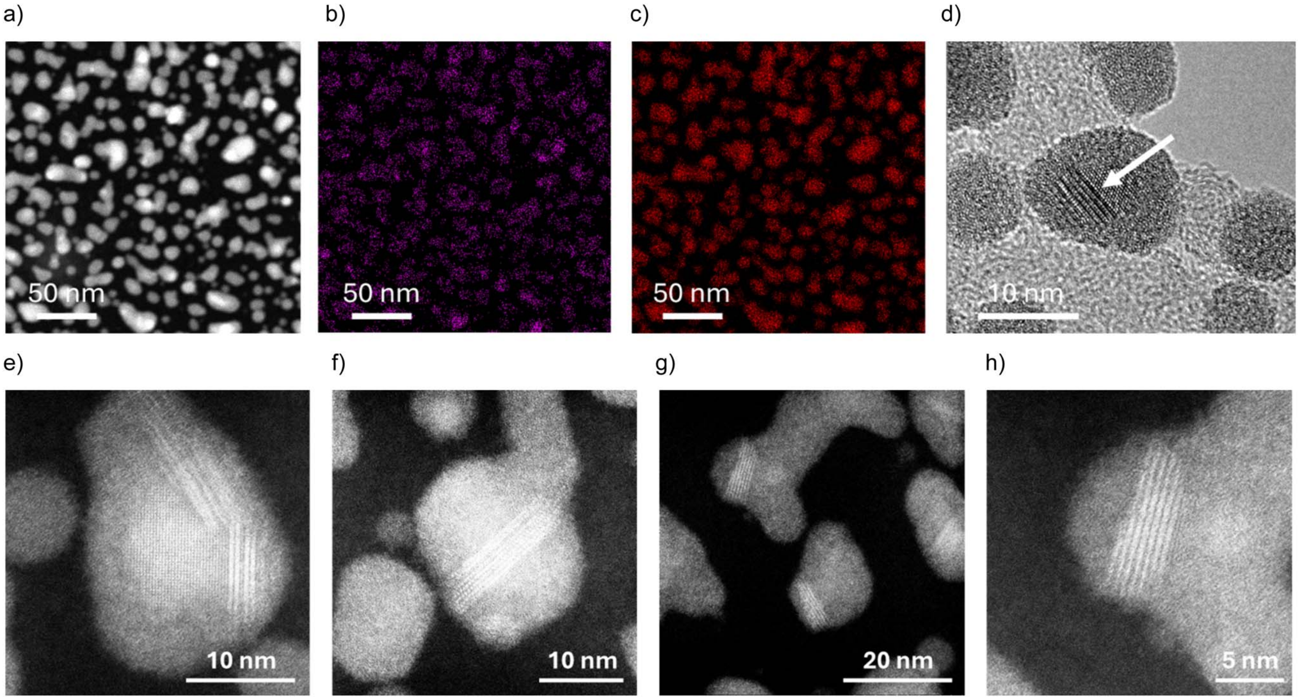

Fig. 5 (a) HAADF-STEM image of the material obtained with the sintered cathode configuration. (b) STEM-EDX map of Pt. (c) STEM-EDX map of Sn. (d) High-resolution TEM image showing a 2D layered phase embedded in Sn particle. (e–h) HAADF-STEM images emphasizing the presence of the layered phase, breaking the spherical symmetry of the particles. (h) Enlarged section of the upper left part of image (g).

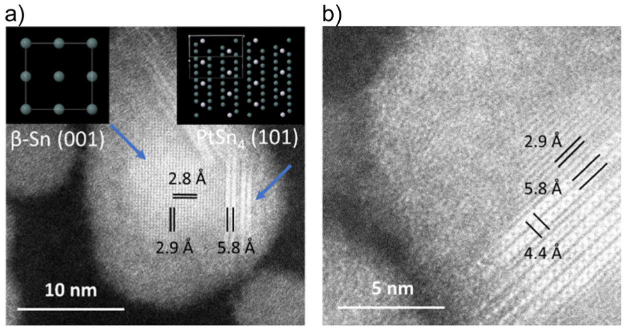

Fig. 7 (a) High-resolution HAADF-STEM analysis of the particle in Fig. 5e. A square-like pattern is observed in the centre of the particle and layered domains on the side, the former with 2.8 and 2.9 Å lattice spacing and the latter with 5.8 and 4.4 Å. The square-like pattern is attributed to the cubic β-Sn metallic phase oriented (001) with respect to the electron beam, and the layered pattern to the intermetallic phase $PtSn_4$ oriented along (101). (b) High-resolution HAADF-STEM analysis of the particle in Fig. 5f.

with respect to the electron beam and β-Sn metallic phase oriented along (001) surrounded by an amorphous, presumably tin oxide phase. Our results agree with the known crystallographic parameters of the intermetallic $PtSn_4$ phase, which crystallizes in the orthorhombic *Ccce* space group and exhibits a layered structure composed of $PtSn_4$ sheets oriented along the (010) direction. In this structure, each Pt atom is 8-coordinated and bonded to eight equivalent Sn atoms in a distorted square antiprism geometry, with four shorter Pt–Sn bonds (2.80 Å) and four slightly longer ones (2.81 Å).

Discussion

Formation of a 2D intermetallic $PtSn_4$ phase

The identification of the 2D layered intermetallic domains with the $PtSn_4$ phase in the nanogranular films by SCBD is a result of paramount importance given the Dirac nodal arc semimetal character of this phase,[17,18] which makes it a material of interest for topological physics, electronic transport phenomena, and related potential applications.[25–27] In addition, the layered arrangement of the Pt and Sn atoms of $PtSn_4$ may provide surface active sites with modified electronic states, which suggest catalytic properties in electrochemical reactions such as the hydrogen evolution reaction (HER) and the oxidation processes in fuel cells.[28,29] Considering the reduced amount of platinum, these properties feature $PtSn_4$ a potential catalyst of remarkable interest.

Beynon *et al.* recently reported for the first time on the synthesis of $PtSn_4$ in the form of a crystalline thin film by electron beam evaporation and provided its full characterization, emphasizing the importance of their achievement for quantum technologies.[30] In the framework of low dimensionality systems, nanostructuring provides insights into the evolution of the Dirac nodal arc semimetal character with the dimension of the crystalline domains. However, the synthesis and stabilization of $PtSn_4$ at the nanoscale remain challenging, and studies on its nanostructured forms are still limited.

Based on our results, we hypothesize that Sn and Pt atoms are released contemporarily by the sputtering of the sintered cathode and aggregate in the form of small clusters, which grow by monomer addition and by coalescence, until they reach dimensions of the order of 10 nm. The difference in sputtering yields of Sn and Pt leads to a nanoparticle composition with a large excess of Sn. Given the low melting point of bulk Sn (232 °C) and considering the further decrease to values far below the bulk one for particles with a diameter of about 10 nm,[31] we propose that the nanoparticles remain in the liquid state for long enough to allow the interparticle precipitation of the $PtSn_4$ crystalline phase (Fig. 8a and b), which is believed to exist in the solid state below 520 °C.[24] A temperature above this value can therefore be inferred for the initial bimetallic vapor of Sn and Pt atomic precursors, upstream the aggregation process (step 1 in Fig. 1).

Sn–Pt particle cooling is initially provided by the collisions with argon within the cluster source and subsequently during the supersonic expansion, for a total process duration—from cathode sputtering to supersonic beam formation—of the order of a few hundred microseconds. Although SCBD is sometimes considered an "out of equilibrium" process due to the sudden temperature drop of the supersonic expansion occurring immediately after particle formation and causing the freezing of their structures (for this reason, its potential ability to produce exotic structures is interesting), here we observe that the formation of highly ordered $PtSn_4$ domains has a fast enough dynamic to be compatible with the SCBD process timeframe and characteristics.

Interestingly, the 2D layered nature of the $PtSn_4$ phase not only creates heterostructures that disrupt the spherical symmetry of nanoparticles typically formed in gas aggregation processes, but in many observed instances, rather than being embedded within tin, the $PtSn_4$ phase sharply separates the Sn particles into two distinct parts. As we previously reported for cluster-assembled nanogranular Sn films deposited at room temperature,[4] a similar partial coalescence is observed here as deposition progresses and substrate coverage increases. This can be linked to the dissipation of the kinetic energy of the

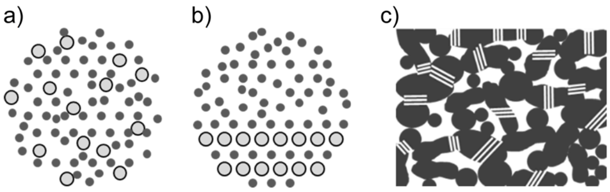

Fig. 8 Schematic representation of Sn–Pt nanoparticles during the cooling process preceding the supersonic expansion. (a) Pt and Sn atoms (light and dark grey dots, respectively) are uniformly distributed in a nanoparticle in the liquid state, where Sn represents the largest component. According to the Sn–Pt phase diagram, the temperature here is expected to be higher than 520 °C. (b) Below 520 °C, the ordered $PtSn_4$ phase precipitates within the still-liquid Sn nanoparticle, which eventually solidifies upon supersonic expansion cooling. (c) Scheme of the possible final structure of the nanoparticle-assembled film where the β-Sn metallic nanogranular network (dark grey) is sectioned by $PtSn_4$ layered domains (white).

particles within the supersonic argon beam, in combination with the reduced melting point of the material. As the deposition proceeds, this partial coalescence leads to the formation of an interconnected nanogranular network, with $PtSn_4$ layered domains segmenting the β-Sn metallic phase, as shown schematically in Fig. 8c. Given that this configuration incorporates units with an alleged Dirac nodal arc semimetal character that interrupt the nanogranular metallic network, we believe that the electrical transport properties of this system warrant specific *in situ* investigations.

Opportunities for chemoresistive gas sensing

The structure of the nanogranular films obtained with the "double rod" cathode configuration, in which the close coexistence of Sn oxide and Pt nanoparticles is observed, suggests a potential use as an active layer in chemoresistive gas sensing applications. Pt nanoparticles with a dimension of about 1 nm, located in close contact with the Sn oxide, are in fact expected to catalytically promote the reactions between airborne chemical compounds and chemisorbed species on the oxide surface, which are at the base of chemoresistive gas sensing mechanism.[32] Preliminary experiments of electrical transport in pure air and in a reactive atmosphere (1% H_2 in air) at different temperatures have been carried out. Assuming that the nanogranular film behaves like the n-type semiconductor SnO_2, the Arrhenius plot analysis of the baseline current *vs.* the temperature (Fig. 9) suggests the presence of donor states characterized by an activation energy for DC conduction of 0.18 eV.

Gas sensing results show an interesting trend of the response to hydrogen exposure with temperature, where a qualitative reversal of the behaviour appears for $T > 150$ °C (Fig. 10). Up to 150 °C, exposure to hydrogen induces an increase of the electrical conduction of the nanogranular film, in line with what is expected from the chemoresistive mechanism occurring in n-type semiconductor oxide sensing materials, such as SnO_2, exposed to "reducing" gases such as H_2. However, at 200 °C the exposure to hydrogen unveils a more complex behaviour characterized by a first, limited current increase followed by a large decrease, unexpected for an n-type semiconductor oxide exposed to hydrogen. Response and recovery dynamics are temperature-dependent. In particular, recovery time appears to be much longer than the air exposure duration in the measurement protocol (120 s).

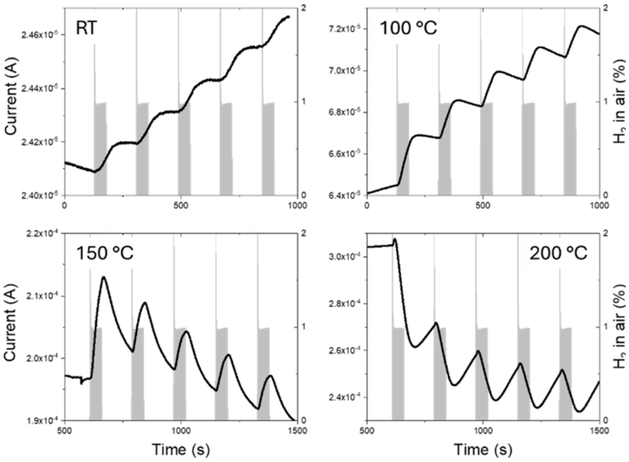

Fig. 10 Hydrogen-induced changes in the electrical transport of the nanogranular film made of segregated families of Sn and Pt particles, at different temperatures. Black curves represent the current across the film at an applied voltage of 100 mV (left axes). Grey bars represent the exposure to hydrogen (right axes). At $T = 200$ °C, the opposite behaviour to that expected from an n-type semiconductor SnO_2 exposed to the reducing gas H_2 is observed.

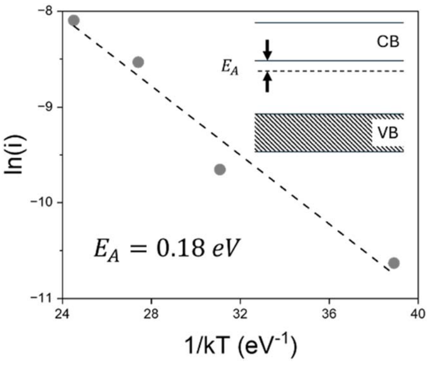

Fig. 9 Arrhenius plot of the baseline current suggesting the presence of donor states characterized by an activation energy of 0.18 eV. VB and CB represent the valence band and the conduction band.

Although these results should be consolidated, especially with respect to additional gas species, they already suggest the possibility of tuning the sensing mechanism according to the operational temperature of the sensing device. This will hopefully contribute to addressing one of the main limitations of metal-oxide gas sensors, *i.e.* selectivity.

Conclusions

In this work, bimetallic nanogranular films combining Sn and Pt were deposited by supersonic cluster beam deposition (SCBD). Their nanostructure can be tuned on one hand towards segregated nanoparticle families of the two metallic species in close contact with one another as if they were originated from a co-deposition process, and, on the other, towards a nanogranular network of metallic Sn "interrupted" by embedded 2D layered intermetallic $PtSn_4$ phases.

The identification of $PtSn_4$ 2D layers, that form spontaneously within Sn nanoparticles of around 10 nm originating in the gas phase process of SCBD, is of remarkable im-portance given the Dirac nodal arc semimetal character of this phase, with implications in the areas of spintronics, magnetoresistance, and topological solid-state physics in general. The transport properties of nanogranular structures embedding a Dirac nodal arc $PtSn_4$ phase deserve dedicated *in situ* investigation during film growth. Phenomena such as quantum tunnelling between non-connected particles at low coverage, the onset and evolution of percolation with increasing coverage, and resistive switching at high coverage may all be affected.

Additionally, *in situ* studies on the material's electronic band structure—examining the relationship between the Dirac semimetal characteristics of $PtSn_4$ and its nanostructured form—could benefit from the possibility of the direct interfacing of the deposition system with surface science facilities thanks to the highly collimated nanoparticle beam and the room temperature deposition process associated with SCBD.

From an applicative perspective, the preliminary results of hydrogen sensing at concentrations below the Low Explosive Limit (LEL, 4% in air) are provided. Qualitative changes in the detection behaviour of the film composed by Sn oxide nanoparticles decorated with 1 nm size catalytic Pt particles are observed at different operating temperatures. The possibility to deposit nanogranular films directly on proper micromachined platforms in one single deposition process can be of great interest for miniaturized gas sensors operating as "edge devices" in Internet of Things (IoT) scenarios.

Author contributions

JEMM prepared all the samples of the study and arranged the SCBD deposition system on purpose, took care of the size distribution characterizations and of the electrical transport measurements in presence of hydrogen. He revised the manuscript. MH performed TEM and STEM-EDX analyses at Juelich and identified the 2D layered phase as $PtSn_4$. He revised the manuscript. AMP performed TEM and STEM-EDX analyses at LIST. He revised the manuscript. EB received the funding for this study, coordinated the team and the experimental work, wrote the manuscript.

Conflicts of interest

The authors declare no conflict of interest.

Data availability

Electron microscopy images are all available in Zenodo Repository. Link: **https://zenodo.org/records/15365098**, DOI: **https://doi.org/10.5281/zenodo.15365098**.

Acknowledgements

This work is supported by the Luxembourg National Research Fund (FNR), CLASMARTS project (C19/MS/13685974), and by SNOX project (ER-C E-002). M. H. thanks Hitachi High-Technology for support. Authors thank L. Stokes for the valuable contribution to manuscript revision.

References

1 F. Borghi, M. Milani, L. G. Bettini, A. Podestà and P. Milani, Quantitative characterization of the interfacial morphology and bulk porosity of nanoporous cluster-assembled carbon thin films, *Appl. Surf. Sci.*, 2019, **479**, 395–402, DOI: **10.1016/j.apsusc.2019.02.066**.

2 A. Del Giudice, G. Benetti, C. Piazzoni and F. Borghi, Porosity of Nanostructured Carbon Thin Films, in *Nanoporous Carbons for Soft and Flexible Energy Devices. Carbon Materials: Chemistry and Physics*, ed. Borghi, F., Soavi, F. and Milani, P., Springer, Cham, 2022, vol 11, DOI: **10.1007/978-3-030-81827-2_8**.

3 E. Barborini, G. Corbelli, G. Bertolini, *et al.*, The Influence of Nanoscale Morphology on the Resistivity of Cluster-Assembled Nanostructured Metallic Thin Films, *New J. Phys.*, 2010, **12**, 073001, DOI: **10.1088/1367-2630/12/7/073001**.

4 J. E. Martinez Medina, J. Polesel-Maris, A. M. Philippe, P. Grysan, N. Bousri, S. Girod and E. Barborini, The role of coalescence and ballistic growth on in-situ electrical conduction of cluster-assembled nanostructured Sn films, *Appl. Surf. Sci.*, 2024, **664**, 160268, DOI: **10.1016/j.apsusc.2024.160268**.

5 G. Nadalini, F. Borghi, T. Košutová, A. Falqui, N. Ludwig and P. Milani, Engineering the structural and electrical interplay of nanostructured Au resistive switching networks by controlling the forming process, *Sci. Rep.*, 2023, **13**, 19713, DOI: **10.1038/s41598-023-46990-4**.

6 Z. Huo, W. Yang, J. Harati, A. Nene, F. Borghi, C. Piazzoni, P. Milani, S. Guo, M. Galluzzi and D. Boraschi, Biomechanics of Macrophages on Disordered Surface Nanotopography, *ACS Appl. Mater. Interfaces*, 2024, **16**(21), 27164–27176, DOI: **10.1021/acsami.4c04330**.

7 E. Barborini. Microhotplates and Integration with Metal Oxide Nanomaterials, in *Metal Oxide Nanomaterials for Chemical Sensors*, ed. M. A. C. S. Mathur and A. Kolmakov, Integrated Micro-analytical Systems, Springer, 2013, pp. 503–537, DOI: **10.1007/978-1-4614-5395-6_16**.

8 V. Gnatkovsky, A. Cattalini, A. Antonini, L. Spreafico, M. Saini, F. Noè, C. Alessi, L. Librizzi, L. Uva, C. E. Marras, M. de Curtis and S. A. Ferrari, Recording Electrical Brain Activity with Novel Stretchable Electrodes Based on Supersonic Cluster Beam Implantation Nanotechnology on Conformable Polymers, *Int. J. Nanomed.*, 2019, **14**, 10079–10089, DOI: **10.2147/IJN.S224243**.

9 J. Sarnthein, K. Seidel, M. C. Neidert, A. Raabe, F. Sala, J. C. Tonn, N. Thon and A. Szelenyi, Evaluation of a new cortical strip electrode for intraoperative somatosensory monitoring during perirolandic brain surgery, *Clin. Neurophysiol.*, 2022, **142**, 44–51, DOI: **10.1016/j.clinph.2022.07.497**.

10 C. Schulte, A. Podestà, C. Lenardi, G. Tedeschi and P. Milani, Quantitative Control of Protein and Cell Interaction with Nanostructured Surfaces by Cluster Assembling, *Acc. Chem. Res.*, 2017, **50**, 231–239, DOI: **10.1021/acs.accounts.6b00433**.

11 E. Barborini, G. Bertolini, M. Epifanio, A. Yavorskyy, S. Vinati and M. Baumann, Cluster-Assembled Nanoporous Super-Hydrophilic Smart Surfaces for On-Target Capturing and Processing of Biological Samples for Multi-Dimensional MALDI-MS, *Molecules*, 2022, **27**, 4237, DOI: **10.3390/molecules27134237**.

12 A. Halder, C. Lenardi, J. Timoshenko, *et al.*, CO2 Methanation on Cu-Cluster Decorated Zirconia Supports

with Different Morphology: A Combined Experimental In Situ GIXANES/GISAXS, Ex Situ XPS and Theoretical DFT Study, *ACS Catal.*, 2021, **11**(10), 6210–6224, DOI: 10.1021/acscatal.0c05029.

13 S. Osmani, E. Scattolin, M. Vergari, A. Gasparotto, G. A. Rizzi and L. Gavioli, The effect of surface states accumulation on photo-electrochemical performances of Bi24Fe2O39 grown by supersonic beams, *J. Phys. Chem. Solids*, 2024, **193**, 112160, DOI: 10.1016/j.jpcs.2024.112160.

14 A. Casu, C. Melis, G. Divitini, F. Profumo, M. Lizzano, F. Borghi, Y. P. Ivanov, R. Dettori, L. Colombo, P. Milani and A. Falqui, An In Situ TEM Study of the Diffusivity of Gold Atoms in Nanocomposite Thin Films by Zirconia Co-Deposition: Implication for Neuromorphic Devices, *ACS Appl. Nano Mater.*, 2025, **8**(4), 1762–1772, DOI: 10.1021/acsanm.4c05993.

15 E. Barborini and S. Vinati, Supersonic Cluster Beam Deposition for the integration of functional nanostructured films in devices, in *Advances in Fabrication and Investigation of Nanomaterials for Industrial Applications*, ed. S. Krishnamoorthy and K. Iniewski, Springer-Nature, Switzerland AG, 2024, DOI: 10.1007/978-3-031-42700-8_1.

16 F. Vega, J. Fernandez, S. Elgueta, E. Cavaliere, L. Gavioli and A. L. Cabrera, Hydrogen adsorption study on nanostructured Ag–Rh films grown by supersonic cluster beam deposition, *Int. J. Hydrogen Energy*, 2023, **48**(45), 17230–17236, DOI: 10.1016/j.ijhydene.2023.01.225.

17 Y. Wu, L.-L. Wang, E. Mun, D. D. Johnson, D. X. Mou, L. Huang, A. Kaminski, *et al.*, Dirac node arcs in $PtSn_4$, *Nat. Phys.*, 2016, **12**(7), 667–671, DOI: 10.1038/nphys3712.

18 N. Kumar, S. N. Guin, K. Manna, C. Shekhar and C. Felser, Topological Quantum Materials from the Viewpoint of Chemistry, *Chem. Rev.*, 2021, **121**(5), 2780–2815, DOI: 10.1021/acs.chemrev.0c00732.

19 E. Barborini, P. Piseri and P. Milani, A pulsed microplasma source of high intensity supersonic carbon cluster beams, *J. Phys. D: Appl. Phys.*, 1999, **32**, L105, DOI: 10.1088/0022-3727/32/21/102.

20 M. Heggen, J. E. Martinez Medina, A. M. Philippe and E. Barborini, Experimental insights on the stability of core–shell structure in single Sn/SnOx spherical nanoparticles during room temperature oxidation, *Appl. Surf. Sci.*, 2025, **684**, 161984, DOI: 10.1016/j.apsusc.2024.161984.

21 J. E. Martinez Medina, A. M. Philippe, J. Guillot, C. Vergne, Y. Fleming and E. Barborini, Intermediate tin oxide in stable core-shell structures by room temperature oxidation of cluster-assembled nanostructured Sn films, *Appl. Surf. Sci.*, 2024, **658**, 159846, DOI: 10.1016/j.apsusc.2024.159846.

22 P. Milani and S. Iannotta, *Cluster Beam Synthesis of Nanostructured Materials*, Springer-Verlag, Berlin Heidelberg, 1999, DOI: 10.1007/978-3-642-59899-9.

23 *Gas-phase Synthesis of Nanoparticles*, ed. Y. Huttel, John Wiley and Sons, 2017, ISBN: 978-3-527-34060-6.

24 R. W. Cahn, Binary Alloy Phase Diagrams–Second edition, ed. T. B. Massalski, Editor-in-Chief; H. Okamoto, P. R. Subramanian, L. Kacprzak, Editors. ASM International, Materials Park, Ohio, USA. 1990, *Adv. Mater.*, 1991, **3**(12), 628–629, DOI: 10.1002/adma.19910031215.

25 X. Luo, R. C. Xiao, F. C. Chen, J. Yan, Q. L. Pei, Y. Sun, W. J. Lu 1, P. Tong, Z. G. Sheng, X. B. Zhu, W. H. Song and Y. P. Sun, Origin of the extremely large magnetoresistance in topological semimetal PtSn4, *Phys. Rev. B*, 2018, **97**, 205132, DOI: 10.1103/PhysRevB.97.205132.

26 E. Mun, H. Ko, G. J. Miller, G. D. Samolyuk, S. L. Bud'ko and P. C. Canfield, Magnetic field effects on transport properties of PtSn4, *Phys. Rev. B: Condens. Matter Mater. Phys.*, 2012, **85**, 035135, DOI: 10.1103/PhysRevB.85.035135.

27 C. Fu, J. Sun, Y. Liu, Y. Jing, X. Xu, X. Chen, X. Zhao, *et al.*, Largely suppressed magneto-thermal conductivity and enhanced thermoelectric performance in $PtSn_4$, *Nat. Commun.*, 2020, **11**(1), 1–8, DOI: 10.34133/2020/4643507.

28 G. Li, C. Fu, W. Shi, L. Jiao, J. Wu, Q. Yang, R. Saha, M. E. Kamminga, A. K. Srivastava, E. Liu, A. N. Yazdani, N. Kumar, J. Zhang, G. R. Blake, X. Liu, M. Fahlman, S. Wirth, G. Auffermann, J. Gooth, S. Parkin, V. Madhavan, X. Feng, Y. Sun and C. Felser, Dirac Nodal Arc Semimetal PtSn4: An Ideal Platform for Understanding Surface Properties and Catalysis for Hydrogen Evolution, *Angew. Chem., Int. Ed.*, 2019, **58**, 13107, DOI: 10.1002/anie.201906109.

29 D. W. Boukhvalov, A. Marchionni, J. Filippi, C.-N. Kuo, J. Fujii, R. Edla, S. Nappini, G. D'Olimpio, L. Ottaviano, C. S. Lue, P. Torelli, F. Vizza and A. Politano, Efficient hydrogen evolution reaction with platinum stannide PtSn4 via surface oxidation, *J. Mater. Chem. A*, 2020, **8**, 2349–2355, DOI: 10.1039/C9TA10097K.

30 E. L. Beynon, O. J. Barker, T. D. Veal, L. O'Brien and M. O'Sullivan, Heterostructure growth, electrical transport and electronic structure of crystalline Dirac nodal arc semimetal PtSn4, *Sci. Rep.*, 2024, **14**(1), 30887, DOI: 10.1038/s41598-024-81679-2.

31 S. L. Lai, J. Y. Guo, V. Petrova, G. Ramanath and L. H. Allen, Size-Dependent Melting Properties of Small Tin Particles: Nanocalorimetric Measurements, *Phys. Rev. Lett.*, 1996, **77**, 99, DOI: 10.1103/PhysRevLett.77.99.

32 R. Leturcq, R. Bhusari and E. Barborini, Physical mechanisms underpinning conductometric gas sensing properties of metal oxide nanostructures, *Adv. Phys.: X*, 2022, **7**(1), 2044904, DOI: 10.1080/23746149.2022.2044904.